Chemical Physics 239 (1998) 525–547

Chemical Physics

Modeling structure and dynamics of solvated molecular ions: Photodissociation and recombination in $I_2^-(CO_2)_n$

J. Faeder, N. Delaney, P.E. Maslen [1], R. Parson

JILA, University of Colorado and National Institute of Standards and Technology, and Department of Chemistry and Biochemistry, University of Colorado, Boulder, CO 80309-0440, USA

Received 4 May 1998

Abstract

We describe a method for simulating the reaction dynamics of a molecular ion embedded in a cluster of polarizable solvent molecules. Potential energy surfaces for ground and excited states are calculated from an effective Hamiltonian that takes into account the strong perturbation of the solute electronic structure by the solvent. The parameters of the model Hamiltonian are obtained from a combination of ab initio calculations and spectroscopic data; intermolecular electrostatic and polarization interactions are treated by the distributed multipole analysis of Stone and co-workers, while short range interactions are modeled with empirical pair potentials. Analytical expressions for the derivatives of the effective Hamiltonian allow for efficient computation of forces and nonadiabatic couplings. The intramolecular degrees of freedom of the solvent molecules are held fixed during the simulations using the method of constraints, and electronic transitions are treated using Tully's surface hopping algorithm. The method is applied to the photodissociation and recombination of $I_2^-(CO_2)_n$. Electronic relaxation in this system is found to occur on multiple time scales, ranging from 2 ps to many tens of ps. The relationship of these results with the experimental measurements of Lineberger and co-workers is discussed.

1. Introduction

The photodissociation and recombination of dihalide ions in gas-phase clusters [1–11] and in liquid solution [12–15] involves dynamics that take place on multiple potential energy surfaces over a wide range of solute bond lengths, solvent configurations, and time scales. Such systems present serious challenges to molecular dynamics simulation. Since photodissociation occurs on an excited electronic state, an accurate treatment of the solute molecule's electronic structure is required, and, since recombination involves transitions to other states, a method for handling electronically nonadiabatic effects is needed. Ionic solutes are more difficult to treat than neutral ones because their electronic structure is strongly perturbed by the coulombic interactions with the permanent and induced moments on the solvent molecules, giving rise to a flow of charge within the solute that is intimately coupled to the dynamics of the solvent. Furthermore, this charge flow is state-dependent: in the ground state the excess charge localizes on the more heavily solvated atom as the

[1] Current address: Department of Chemistry, University of California, Berkeley, CA 94720, USA.

0301-0104/98/$ - see front matter
PII: S0301-0104(98)00309-7

molecule dissociates, but in certain excited states the charge flows in the opposite direction [16,17]. Because of these complications, theoretical treatments have until recently dealt with limited aspects of the problem such as vibrational relaxation in the electronic ground state [17–20].

In the past two years, the development of convenient and accurate model Hamiltonians for the interacting solute-solvent system has made simulations of the full dynamics possible. Batista and Coker [21] have used a semiempirical Diatomics-in-Ionic-Systems Hamiltonian to simulate the photodissociation and recombination of I_2^- in Ar clusters, and have achieved good agreement with the experimental product distributions [7]. Our own group has developed a model Hamiltonian based on ab initio electronic structure calculations and the distributed multipole analysis of Stone and co-workers [22], with which we have successfully reproduced the observed product distributions in I_2^- clustered with Ar [23] and CO_2 [24], and the time-resolved photoelectron spectra of $I_2^-Ar_n$ clusters [25]. The present paper is the second of two devoted to describing this model in full detail. In the first paper [26] we derived an effective Hamiltonian for the electronic structure of a charged solute embedded in a cluster of polarizable solvent molecules. Here we show how the parameters in this Hamiltonian are determined from a combination of ab initio and experimental data, and how the Hamiltonian is used to compute cluster structures and dynamics. We use $I_2^-(CO_2)_n$ to illustrate the procedure since this is the most extensively studied experimental system in this class, but the model has also been applied to several other diatomic solute-solvent systems [27]. The only fundamental restriction is that charge transfer or chemical reaction between solute and solvent not be important in the excitation energy range of interest.

The paper is constructed as follows: Section 2 describes the electronic structure of I_2^- in the gas phase, emphasizing aspects of the electronic structure that are important for modeling the solute-solvent interactions. Section 3 describes the potential model for I_2^- embedded in a CO_2 cluster. The main goal here is to incorporate experimentally known features of the potentials with an accurate treatment of the electrostatic interactions, which dominate because of the excess solute charge. The ab initio wave functions of the solute, parameterized in terms of distributed multipole operators, provide the basis for determining the electrostatic interactions between the solute and solvent. The solvent is treated in a more empirical fashion, using distributed charges, point polarizabilities, and pair potentials. Section 4 shows how structural and dynamical properties are calculated from the effective Hamiltonian. Methods for computing minimum energy cluster structures, adiabatic dynamics on single potential energy surfaces, and nonadiabatic transitions among potential surfaces are described. A central advantage of our model is that derivatives of the effective Hamiltonian, and thereby forces and nonadiabatic transition probabilities, are obtained in a convenient analytic form; the formulas that we use are given at the end of Section 4. In Section 5 the model is illustrated with simulations of photodissociation and recombination in $I_2^-(CO_2)_n$ clusters. We have presented some of these results in an earlier communication [24]; in the present paper we discuss in more detail the time scales for electronic relaxation and their relationship to the time-resolved experiments of Lineberger and co-workers [2,4,5].

2. Electronic structure of I_2^-

In an earlier paper [28] we have reported multireference configuration interaction (MRCI) calculations of the ground and excited states of I_2^- and ICl^-. We summarize here those aspects of the electronic structure that are important for understanding the interaction between the dihalde anion and a solvent.

The dihalide anions, one electron short of a complete valence shell, behave like one-electron molecules, with the position of the hole determining the symmetry of the electronic state. Considering the valence s electrons as occupying a closed subshell, there are 11 valence p electrons that must be placed into 6 valence p orbitals—σ, π, π^*, and σ^*—as shown in the orbital correlation diagram of Fig. 1. In the absence of spin-orbit splitting, there are four distinct energy levels arising from a total of 12 molecular states, 2 $^2\Sigma$ and 2 $^2\Pi$, which all dissociate to give a ^2P halogen atom and a ^1S halide anion. We refer to these as the case (a) states. The potential curves for these states in I_2^-, shown in Fig. 2(a),

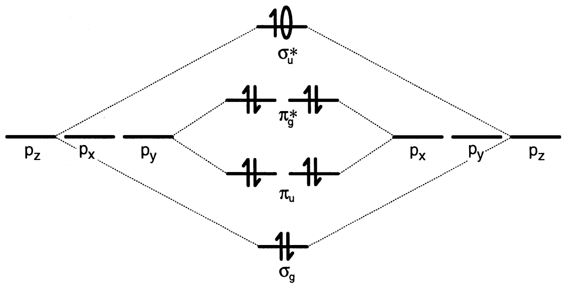

Fig. 1. Orbital correlation diagram for X_2^- without spin-orbit coupling [Hund's case (a)]. There are six doublet states corresponding to the electron hole occupying one of the six valence orbitals. The symmetry of the total wave function is simply that of the orbital containing the hole.

illustrate several important points. First, there is a strong attraction in the Σ bonding state, while the remaining curves are repulsive or only slightly attractive. Second, the Σ^* antibonding state lies above the Π^* antibonding state at the equilibrium bond length, R_e, which strongly influences the character of the spin-orbit coupled excited states, as discussed below. Finally, there is a crossing between the Σ^* and Π^* states at intermediate bond lengths, which is due to the interaction between the positive quadrupole moment of the neutral atom and the negative charge of the ion. This interaction is attractive for the Σ states, and repulsive for the Π states.

In addition to being useful for understanding the electronic structure of these anions, the case (a) states are convenient for calculations because most ab initio programs do not include spin-orbit coupling. In our approach the case (a) states are determined using the ab initio program MOLPRO [29]. The matrix elements of a semiempirical spin-orbit operator (parametrized by atomic spin-orbit coupling constants) are evaluated in these basis states, and the resulting Hamiltonian is diagonalized to give the fully coupled electronic eigenstates of the isolated molecule. Spin-orbit coupling splits the four Hund's case (a) levels into six and lifts the degeneracy of the atomic $^2P_{3/2}$ and $^2P_{1/2}$ states, as illustrated in Fig. 2(b). An orbital correlation diagram based on the Hund's case (c) atomic states is shown in Fig. 3. Although the Hund's case (a) labels are still used to describe the curves, the only good quantum numbers

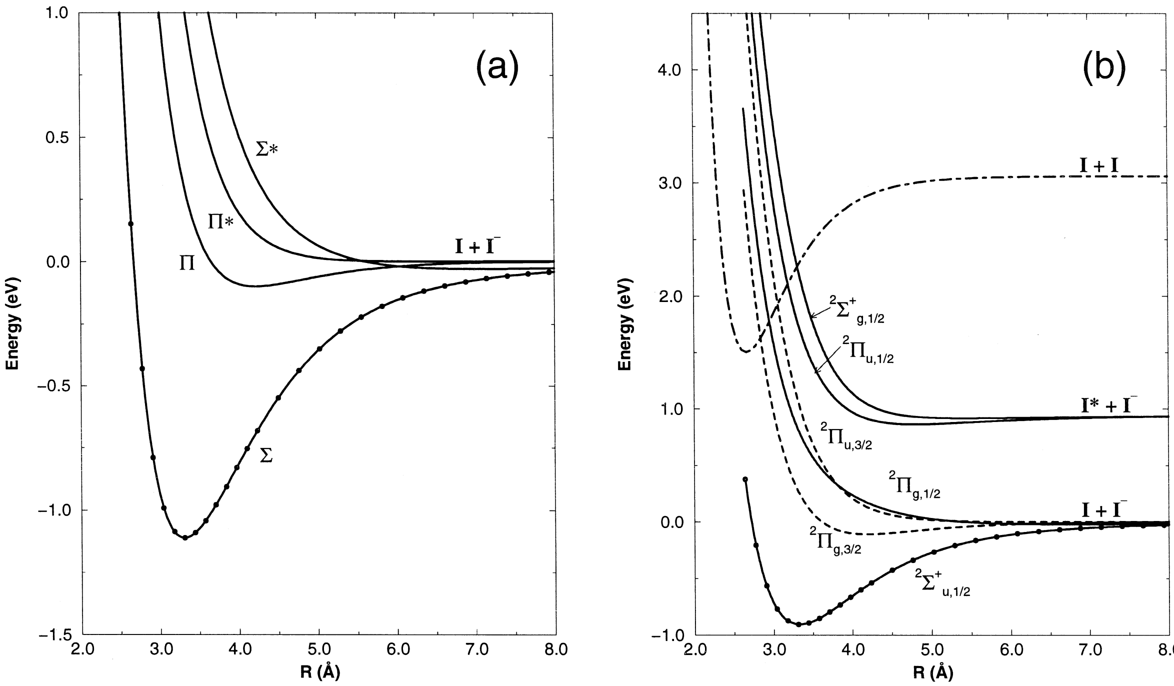

Fig. 2. Ab initio potential curves for I_2^-. (a) Without spin-orbit. (b) Including spin-orbit coupling. The Hund's case (a) labels used in (b) are approximately valid near R_e, but become inappropriate as the bond dissociates. Parameters for the neutral curves were taken from Ref. [83].

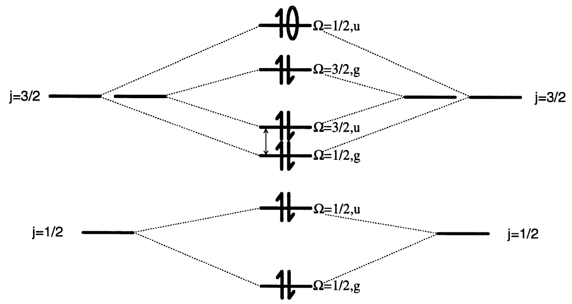

Fig. 3. Orbital correlation diagram for X_2^- including spin-orbit coupling [Hund's case (c)]. There are six doublet states corresponding to the electron hole occupying one of the six valence orbitals. As the bond coupling increases, the orbitals indicated by the arrow cross because the upper and lower orbitals correlate to bonding and antibonding orbitals respectively.

are Ω, the projection of the total electronic angular momentum onto the internuclear axis, and the g and u parity labels.

At long bond lengths, the case (c) coupling picture completely describes the states of the system. At shorter distances the bonding interaction is comparable to the spin-orbit coupling, so a hybrid of the case (a) and case (c) pictures governs the states. The case (c) states are a mixture of the case (a) states with the dominant case (a) state determining the approximate symmetry label. The dominant case (a) state comprises at least 90% of the wave function at R_e [28], so the case (a) labels provide a good description near the equilibrium bond distance. This mixing at R_e is important experimentally, however, because the transitions that have been used to study these systems (see Fig. 4) rely on mixing of the Σ^* character into one of the Π states for intensity. The perpendicular $\Sigma \to \Pi$ transition is too weak on its own to be used in the experiments, while the parallel $\Sigma \to \Sigma^*$ transition moment is always large. The mixing is also important because the bonding and antibonding character of each state determines the direction of excess charge flow. The importance of the antibonding states for both the transition moments and the charge flow demonstrates the need to include all four of the low-lying case (a) electronic states in the solute Hamiltonian.

Our electronic structure calculations yield a ground state well depth that is about 10% smaller than the experimentally determined value of 1.01 eV [30], presumably because of the limitations of our one-electron basis sets. We have employed a simple scaling procedure to adjust the well to match the experimental values. The adjustment is done on the case (a) curves to avoid extra transformations between the case (a) and case (c) states. In the region near R_e, there is little mixing of the ground case (a) Σ state with the excited states [28]. Therefore, scaling the Σ state has little effect on the energies of the excited states. All of the case (a) states are shifted by the same amount in order to preserve the energy spacings between the states, which agree well with the experiments. The amount of the shift is given by

$$\Delta(R) = \left(\frac{c-1}{2}\right)\left(1 - \tanh\left(\frac{R-R_c}{w_c}\right)\right) \times \left[V^{\Sigma}(R) - V^{\Sigma}(\infty)\right], \quad (1)$$

where the parameters c, R_c, and w_c are chosen to give the correct well depth for the ground state

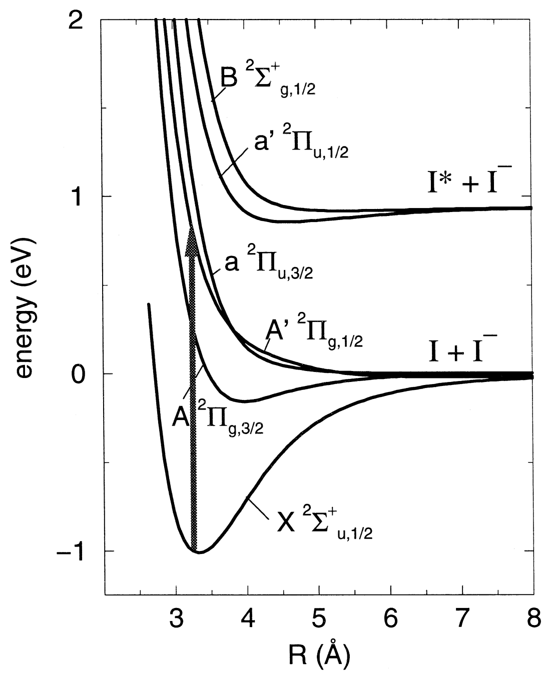

Fig. 4. Scaled potential curves for I_2^-. The ground state has been scaled to match the experimental well depth, while the excited states have been shifted by the same amount to preserve the energy spacings. The transition used to excite the solute in the photodissociation experiments is indicated by the arrow.

without shifting R_e significantly (<0.01 Å). The scaled potential curves are shown in Fig. 4. The excited state curves are all unbound or very weakly bound in comparison with the ground state, as one would expect from simple molecular orbital considerations. Through comparison with the known bond dissociation energies of Xe_2^+, Chen and Wentworth [31,32] have suggested that all of the excited states of I_2^- are slightly bound. Given the limits of the current calculations, we do not expect these wells to be accurately reproduced, and there are differences between our calculated values and the semiempirical fits.

3. Model Hamiltonian for dihalide anions in clusters

The model Hamiltonian is constructed under the assumption that electrostatic and polarization terms will dominate the mixing of different solute states. The remaining terms, arising from dispersion and repulsion, provide the shape and energetics of the short-range interaction potentials:

$$\hat{h}^{\mathrm{eff}} = \hat{h}^{C} + E^{\mathrm{intra}} + \hat{h}^{\mathrm{lr}} + \hat{h}^{\mathrm{sr}}. \tag{2}$$

Here $\hat{h}^{C}$ is the Hamiltonian of the isolated solute and E^{intra} is the total intramolecular energy of the isolated solvent molecules, which is just the sum of their internal energies. $\hat{h}^{\mathrm{lr}}$ contains the long-range electrostatic and polarization terms, while $\hat{h}^{\mathrm{sr}}$ represents the residual short-range interactions. In general the short-range terms depend on the electronic state of the solute, but we expect that if the electrostatic terms are large, as they are in ionic systems, the state dependence will be relatively small—too small to extract from the relatively low resolution spectroscopic data available for ionic and open-shelled systems. We have therefore used empirical state-independent parameters to describe the short-range interactions in most of our applications.

3.1. Long-range interactions

The electrostatic potential arising from a molecular charge distribution may be expanded in a multipole series, the convergence of which may be greatly accelerated by using distributed multipoles (DM) instead of a single-center expansion [22,33,34]. In particular, the distributed expansion converges for points that lie outside of the charge distribution but inside the molecular radius, where the single-center expansion breaks down. In clusters and condensed phases molecules pack closely, so that accurate representation of the electrostatic interactions in this regime is essential. In the DM expansion, several sites, usually atoms and bond centers, are chosen within each molecule, and the multipoles for the entire molecule are partitioned into contributions from each of these sites. At each site the moments are expanded to a given order in real spherical tensor moments [35].

We treat the solvent molecules classically, so their distributed multipole moments are simply classical variables. We have found that distributed charges and single site dipole polarizabilities are adequate for creating realistic interaction potentials. Five charges, taken from Murthy et al. [36], are used for the CO_2 model. These charges reproduce the quadrupole moment of CO_2, and in conjunction with Lennard-Jones sites on the atoms give interaction potentials that reproduce the experimentally observed structures for the dimer and trimer of $(CO_2)_n$ clusters [37]. The polarizability of CO_2 has little effect on the solvent-solvent interactions but has a strong interaction with the solute anion. The model includes a single site on CO_2 with different polarizabilities parallel and perpendicular to the bond. The values for all of the parameters used to describe the solvent charge distribution, the solvent-solvent interactions, and the short range solute-solvent interactions described in the next section are shown in Table 1.

In contrast to the solvent, the solute charge distribution is treated quantum mechanically. Electronic structure calculations provide wave functions for the ground and valence excited states of the isolated solute. From these wave functions we construct the solute charge density matrix, which allows us to determine how the electronic structure of the solute is perturbed by interaction with the solvent. In the representation defined by the isolated solute eigenstates, the diagonal elements of the density matrix represent the charge distribution in particular states while the off-diagonal matrix elements represent

Table 1
Potential parameters $I_2^-(CO_2)_n$

CO_2 geometry		
R_{C-O} (Å)	1.16	
CO_2 charge distribution [a]	charge (au)	distance from C (Å)
$q_1 = q_5$	0.1216	1.523
$q_2 = q_4$	−0.6418	1.066
q_3	1.0404	0.000
CO_2 polarizability [b]		
α_{zz} (Å^3)	4.487	
$\alpha_{xx} = \alpha_{yy}$ (Å^3)	2.127	
Induction damping [c]		
R_{damp} (Å)	2.75	
w_{damp} (Å)	0.529	
LJ parameters	σ (Å)	ϵ (meV)
C–C [a]	2.824	2.256
O–O [a]	3.026	6.477
C–O [a]	2.925	3.823
C–I	3.805	16.33
O–I	3.200	12.56

[a] Ref. [36]. [b] Ref. [82]. [c] See Eq. (6).

transition charge densities, which account for the mixing of the isolated solute states brought about by interaction with the solvent. Transition densities allow the solute charge distribution to polarize in response to the external fields that act on it, and thus enable the model to describe solvent-induced charge localization in terms of delocalized molecular eigenstates.

Just as a classical density is expanded in terms of distributed multipole moments, the quantum density matrix is expanded in terms of distributed multipole *operators* [22]. The matrix elements of these operators are determined for each geometry at which the ab initio wave functions were calculated (a total of 50 internuclear distances for I_2^-). When the bonding interactions are strong, the multipoles are distributed over four sites—one on each nucleus and two at equidistant points along the bond axis. At longer bond lengths, the bond sites are gradually damped using a hyperbolic tangent switching function to reflect the localization of the wave function onto the nuclei. Multipoles through quadrupole must be included at a minimum because the open-shell halogen atoms have substantial quadrupole moments that interact with the solvent. The quadrupole moment for the valence p orbital on I from the ab initio calculation is 17.4 atomic units (2.34 Debye Å).

The absorption spectra discussed in Ref. [28] provide one test of the accuracy of the calculated charge density matrix. We found good agreement with experiment for the magnitudes of the parallel transition moments from the ground electronic state at equilibrium separation, but there is some evidence that the calculated perpendicular transition moments near R_e are too small. Aside from these measurements, the only way to determine if the charge distributions of the dissociating molecule are correct is by comparison of simulations to photofragmentation and pump-probe studies of photodissociation in clusters. The overall agreement is quite good, although these measurements are sensitive to many factors other than the distribution of solute charge, so it is difficult draw conclusions about particular components of the model.

The potential energy associated with the long-range interactions can be partitioned into electrostatic and polarization terms, $\hat{h}^{lr} = \hat{h}^{es} + \hat{h}^{pol}$. The electrostatic energy arises from the interaction between permanent multipoles on solvent and solute:

$$\hat{h}^{es} = \frac{1}{2} \sum_{A_i,B_j,t,u} Q_t^{A_i} T_{tu}^{A_i B_j} Q_u^{B_j} + \sum_{A_i,C_j,t,u} Q_t^{A_i} T_{tu}^{A_i C_j} \hat{q}_u^{C_j}$$

$$\equiv \frac{1}{2}(Q + \hat{q}) \cdot T \cdot (Q + \hat{q}), \quad (3)$$

where the sum runs over the sites and multipole orders on each pair of molecules in the system. The letter ''C'' is reserved for the solute while ''A'' and ''B'' run over solvent molecules. The elements of the interaction tensor T depend on the intermolecular distances and orientations; $T_{tu}^{A_i B_j}$ gives the coordinate dependence of the interaction between the multipole of order t on site i of molecule A and the multipole of order u on site j of molecule B. Although the tensor elements are rather complicated functions for all but the lowest order of multipoles, explicit expressions for them have been tabulated [22,35,38]. Note that $T^{A_i A_j}$ and $T^{C_i C_j}$ are always zero because it is assumed that interactions within a single molecule are accounted for in the intramolecular energy. In the second line of Eq. (3) we have introduced a convenient matrix notation; the rows and column indices of the matrix T include all the expansion sites and multipole components on all molecules in the system.

The polarization energy of the solute-solvent system contains the interactions between permanent and induced moments as well as the mutual interaction between induced moments. It can be expressed as [26]

$$\hat{h}^{\mathrm{pol}} = -\tfrac{1}{2}(Q+\hat{q})\cdot T\cdot\boldsymbol{\chi}\cdot T\cdot(Q+\hat{q}), \tag{4}$$

where $\boldsymbol{\chi}$ is a generalized electric susceptibility matrix, which in the linear response approximation is given by

$$\boldsymbol{\chi} \equiv -\left[T+\boldsymbol{\alpha}^{-1}\right]^{-1} \tag{5}$$

in terms of the polarizabilities $\boldsymbol{\alpha}$ of the solvent molecules. The polarization energy is not pairwise additive because the induced multipoles interact with each other; construction of the susceptibility matrix $\boldsymbol{\chi}$ is equivalent to solving the linear response equations relating permanent and induced moments. This calculation is usually the most computationally demanding step in constructing the effective Hamiltonian. When only a single source term is present, it may be efficient to evaluate the induced moments using an iterative procedure. Because the source term in $\hat{h}^{\mathrm{pol}}$ is an operator, however, a different set of induced moments must be computed for each pair of basis states. In clusters, where the number of polarizable sites is relatively small, it is therefore more efficient to compute $\boldsymbol{\chi}$ directly by inverting the matrix $[T+\boldsymbol{\alpha}^{-1}]$.

A well-known problem in many-body polarization models is the singularity that arises when polarizable sites are too closely spaced [39]. One solution to this problem is to damp the polarization interactions at short bond lengths using a simple radial function,

$$\gamma(R) = \tfrac{1}{2}\left[\tanh\left(\frac{R-R_{\mathrm{damp}}}{w_{\mathrm{damp}}}\right)+1\right], \tag{6}$$

which is applied to each interaction tensor element connecting each pair of polarizable sites [22]. The parameters R_{damp} and w_{damp} are chosen to have a small effect near equilibrium separations but to turn on damping rapidly when the charge clouds are penetrated. Values of these parameters are shown in Table 1.

3.2. Short-range interactions

The basic method of handling the short-range interactions places isotropic, pairwise Lennard-Jones (LJ) sites on all the nuclei with parameters fit to match available experimental data,

$$\hat{H}^{\mathrm{sr}} = \sum_{ij}{}' 4\epsilon_{ij}\left(\frac{\sigma_{ij}^{12}}{R_{ij}^{12}} - \frac{\sigma_{ij}^{6}}{R_{ij}^{6}}\right), \tag{7}$$

where the indices i and j run over all the atomic sites in the system, and the sum is restricted to include only pairs where the sites reside on different molecules. Note that since the charge on each solute atom depends on the solute wave function, having different short-range interactions for the ionic and neutral atoms requires introducing a state-dependent interaction. It is not obvious, however, that a set of LJ parameters that gives a correct overall potential for the $I^- \cdots CO_2$ interaction will also give the correct interaction for $I \cdots CO_2$, because one would expect the presence of the extra electron to change the effective size and shape of the iodide. Our procedure is to start with the simplest empirical description of the potentials, as given by Eq. (7), and modify these as is warranted by the available data. We have found that it is not necessary to change the LJ parameters going from I^- to I in order to fit the experimental interaction potentials. In the case of the $I \cdots Ar$ potentials, however, we found that an anisotropic and state-dependent dispersion term had to be added to reproduce the experimental potential curves [23].

Little is known about the interactions of the diatomic solute with the solvent molecules. An estimate of the binding energy has been obtained from photofragmentation studies [3,7], but no spectroscopic data is yet available. Therefore, all of the solute-solvent potentials are fit to the better-known interactions between the solute fragments and the solvent molecules. Because we include the electrostatic effects at a high level, we assume only that the short-range solute-solvent interactions are not dramatically altered by the chemical bonding within the

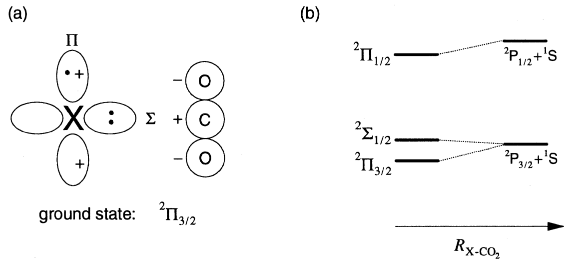

Fig. 5. Interaction of ^2P halogen atom with CO_2. (a) Shows that the state with a hole in the Π orbital is lower in energy because of the resulting positive quadrupole moment, which interacts favorably with the quadrupole on CO_2. In the Σ orientation, the hole interaction with the CO_2 quadrupole is slightly repulsive. (b) Shows the resulting state ordering when spin-orbit coupling is included. The ordering of the lower two states is reversed for the linear geometry.

solute. A combination of scattering data and photoelectron spectroscopy [40,41] has been used to determine potentials for neutral and negatively-charged halogen atoms interacting with various solvent molecules. The bond lengths from these fits are accurate to a few percent, while the binding energies are known to about 5%.

All of the terms used to fit these short-range interactions are pairwise-additive. There is little data for these systems sufficient to resolve the small many-body dispersion terms. The only data on many-body interactions of direct relevance to the model is the study of I^-Ar_n potentials made by Yourshaw et al. [42]. They found that many-body induction was the major contributor to the many-body interaction—about 15% of the total interaction energy—while many-body exchange and dispersion terms had an effect of at most a few percent. Since our model does treat the many-body induction accurately, inclusion of short-ranged nonadditive effects does not seem necessary.

The $I^- \cdots CO_2$ and $I \cdots CO_2$ interaction potentials for the T-shaped configuration are known to good accuracy from ZEKE measurements [40]. The anion is T-shaped because of the strong interaction of the ion with the large CO_2 quadrupole. The electronegative oxygen atoms are repelled strongly by the anion, even forcing CO_2 to bend slightly away from the ion, which has been observed experimentally [43]. In $I^-(CO_2)$ the bending is about 5 degrees. For simplicity we have chosen to keep CO_2 rigid in our simulations; simulations of $I_2^-(CO_2)_n$ dynamics on the electronic ground state using a flexible model for CO_2 found that the bending vibrations had little effect on the adiabatic dynamics [44]. Modeling has indicated that the bending arises mostly from electrostatic effects rather than charge transfer [43]. One might expect that for clusters with more than a few CO_2 molecules, the extent of the bending will be reduced by the solvent-solvent interactions, which favor linear CO_2.

The ZEKE experiments show that the neutral $I \cdots CO_2$ cluster has at least a local minimum in the T-shape geometry. The electrostatic interaction between the halogen atom and CO_2 quadrupoles is proportional to $1/R^5$ and is the leading term in the neutral potential. This term contains the correct anisotropy to describe the splitting of the three observed

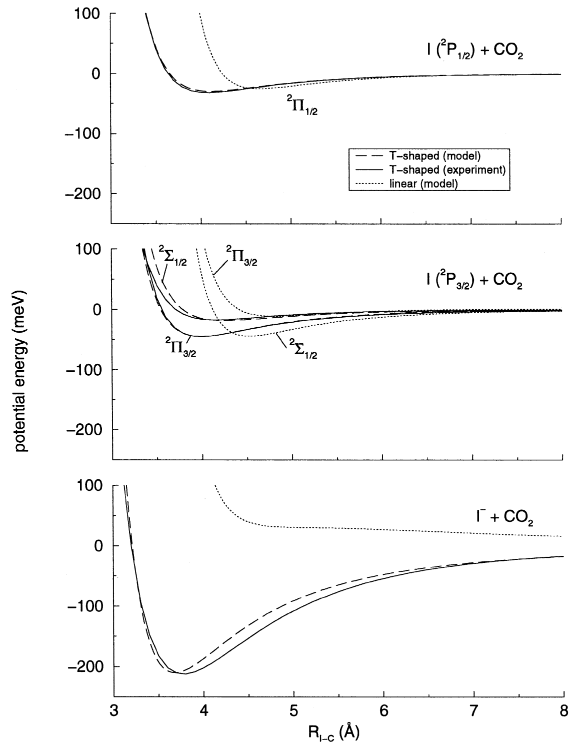

Fig. 6. Potential curves for $I(^2P)$ interacting with CO_2 in the linear and T-shaped geometries. The dashed and solid lines show a comparison between the model and experimental fits. The interaction for the linear geometry of the anion is strongly repulsive, but there are significant attractive wells for the linear configurations of the neutral states.

neutral states. The interactions between the quadrupole on the neutral halogen atom and the quadrupole on CO_2 are illustrated in Fig. 5. The positive halogen quadrupole is parallel to the negative CO_2 quadrupole in the $\Omega = 3/2$ state, resulting in a more attractive interaction than in the $\Omega = 1/2$ state, where the quadrupole-quadrupole interaction is unfavorable. The situation is reversed in the linear geometry.

We have obtained good fits using the four LJ parameters associated with the pairwise atomic interactions in addition to the electrostatic Hamiltonian. The fits to the $I^- \cdots CO_2$ and $I \cdots CO_2$ curves are shown in Fig. 6 and the LJ parameters are given in Table 1.

4. Methods for computing structure and dynamics

The preceding section presented an effective Hamiltonian for the electronic states of a solute embedded in a molecular cluster or solvent. The eigenvalues of this Hamiltonian are functions of the nuclear positions, and define the Born-Oppenheimer potential surfaces that govern the nuclear motion. For photodissociation we want to model the dynamics that occur when the solute in its ground electronic state absorbs a photon and is excited to a potential surface on which the solute nuclei are repelled. Because there are many nuclear degrees of freedom in the cluster, the nuclear dynamics on each potential surface are treated classically, by solving Newton's equations of motion for the nuclei under the influence of the Born-Oppenheimer potential surface.

The initial configurations of the cluster prior to photoexcitation are determined from molecular dynamics (MD) simulations on the ground state potential surface. Trajectories are initiated from an arbitrary configuration at a fixed total energy, and are followed until the distribution of energy throughout the cluster reaches equilibrium. After equilibration, cluster configurations are periodically sampled to construct an ensemble of starting points for photodissociation trajectories. The ensemble is meant to sample the range of initial configurations sampled by an experiment performed under specific conditions, most often at fixed temperature.

Following photoexcitation, the solute nuclei fly apart on the repulsive excited state surface. As the solute nears dissociation, its electronic states bunch together, leading to a breakdown of the Born-Oppenheimer picture. The electrons of the solute no longer respond instantly to the motions of the nuclei, so that the true electronic wave function of the solute becomes a mixture of the adiabatic states. The simulations reported here were performed using a surface-hopping (SH) approach to describe the nonadiabatic dynamics. The nuclei evolve on a single adiabatic state at a time, but this state can change when nonadiabatic coupling with other states occurs. Surface hopping is determined stochastically according to an algorithm in which the probability of occupying each adiabatic state is given by the square of its amplitude in the total nonadiabatic electronic wave function. Because this is an all-or-nothing approach —the trajectory must always be on one surface or another—a large number of trajectories must be computed to determine the correct branching probabilities into each of the coupled states.

4.1. Adiabatic dynamics

It is common practice in MD simulations to constrain those intramolecular degrees of freedom that are not considered vital to the properties of interest, so that a larger time step can then be used in integrating the equations of motion. The simulations presented here have treated the solvent molecules as rigid, and the good agreement of the results with experiment suggest that this is a reasonable approximation. In the future it will be important to study the effects of relaxing the internal molecular constraints to determine what role intramolecular vibrations play in dissipating excess vibrational and electronic energy due to photoexcitation.

Our procedure for constraining the intramolecular degrees of freedom is based upon the work of Ciccotti, Ryckaert and coworkers [45–48]. The molecular geometry is specified by the Cartesian coordinates of a core group of atoms, and holonomic constraints are applied to selected bond distances and dihedral angles. Constraining all of the core atom distances fixes the molecule as rigid; semirigid molecules can be treated by replacing individual constraints with internal potentials. The most expensive part of most molecular models is the evaluation of energies and forces (particularly when there are non-additive contributions, as there are in our model), and overhead associated with integrating the additional equations of motion or applying constraints is usually small. What is most important is picking an integration method that yields acceptable accuracy for a maximal step size, so that the number of force evaluations can be limited. The Verlet algorithm [49] and its descendant the velocity Verlet algorithm [50], which we have used, provide an optimal balance between efficiency and accuracy [51].

The method of constraints specifies three site categories: primary atom, secondary atom, and force center. The primary atoms define each subunit, and their coordinates are used to integrate the equations of motion. All forces and torques in the system must be converted to forces on the primary atoms. Our model for rigid CO_2 has the two primary oxygen atoms, a secondary carbon atom at the bond midpoint, and a bond constraint fixing the O–O distance at r_{O-O} (Fig. 7). Five additional force centers for the point charges and one additional force center for the polarizability along with the pairwise Lennard-Jones interactions associated with the atomic sites complete the potential model described in Section 3. Because the polarizability of CO_2 is anisotropic, the polarizable site exerts a torque on the molecule, which is resolved into forces on the primary atoms using the derivatives of the molecular axes with respect to the primary atom positions. Methods for resolving these torques and for determining the forces due to multipole sites of arbitrary order are discussed in Section 4.3.3 and in Ref. [27].

The model for the diatomic solute consists of two primary atoms and four force centers for the multipoles located on the nuclei and at equidistant points along the bond. The internal potential of the molecule is built into the effective Hamiltonian described in Section 3. As in the CO_2 model, the primary atomic sites are also associated with pairwise Lennard-Jones potentials that describe the short-range interactions with the solvent atoms.

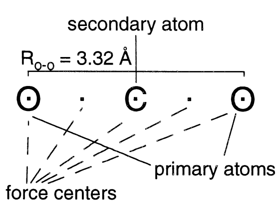

Fig. 7. Rigid CO_2 model using method of constraints.

In characterizing the behavior of clusters at equilibrium, it is useful to identify local minima of the potential surface [52] since structural features of these minima often influence the dynamics both before and after photoexcitation. We find minimum energy structures using standard optimization techniques [53]. Two features must be added to these algorithms to ensure that the constraints are obeyed while retaining the efficiency of the method. First, the constraints must be projected out of the gradient or force vector, so that infinitesimal displacements along the gradient do not violate the constraints. Second, one must devise a method for applying the constraints to configurations where the constraints are violated by a small amount, which arise because the constraints are in general not linear with respect to the displacements. Our implementation is based on the projection operator method described by Lu, Zhao, and Truhlar [54]. These workers combined projected constraints with quasi-Newton optimization algorithms, while we have used both quasi-Newton and conjugate gradient techniques to find minima. Conjugate gradient methods are advantageous when the derivatives are expensive to compute; however, for our model Hamiltonian, evaluation of the forces analytically is only about three times as expensive as evaluation of the energy alone, and we have found that the quasi-Newton [53], or variable metric methods give substantially better performance. Both methods are faster than the simulated annealing techniques using Monte Carlo trajectories previously used by our group [3,17] and molecular dynamics quenching [55,56], which we have also tested.

4.2. Nonadiabatic dynamics

Photodissociation in molecular clusters involves dynamics on multiple potential energy surfaces. A complete description of such a process would require quantum-mechanical treatment of both the nuclear and electronic degrees of freedom, which is not feasible for systems with more than a few atoms. Mixed quantum-classical (MQC) methods, in which the majority of degrees of freedom are described by classical mechanics, offer an attractive alternative since they scale linearly with number of degrees of freedom. Central to all MQC methods is the concept of a path through configuration space followed by the classical degrees of freedom under the influence of forces determined from both the classical and quantum systems. The time evolution of the quantum wave function is determined by integrating the time-dependent Schrödinger equation along the classical path. The Hamiltonian for the system is expressed as an operator on the quantized electronic coordinates $\mathbf{r}$ that depends parametrically on the classical nuclear coordinates $\mathbf{R}(\mathbf{t})$:

$$\hat{H} = \hat{H}_0(\mathbf{r};\mathbf{R}) + \hat{T}(\mathbf{R}), \tag{8}$$

where $\hat{H}_0(\mathbf{r};\mathbf{R})$ is the Hamiltonian for fixed nuclei and $\hat{T}(\mathbf{R})$ is the nuclear kinetic energy operator. The wave function for the quantum subsystem is expanded in a basis of orthonormal functions that also depend parametrically upon the nuclear coordinates:

$$\Psi(\mathbf{r},\mathbf{R},t) = \sum_i c_i(t)\,\psi_i(\mathbf{r};\mathbf{R}). \tag{9}$$

Putting this wave function into the time-dependent Schrödinger equation yields an equation of motion for the quantum amplitudes $c_i(t)$. It is convenient to choose the eigenstates of $\hat{H}_0$ as a basis since this representation can be uniquely defined for a general system. In this ''adiabatic'' representation the quantum amplitudes obey

$$i\hbar\dot{c}_i(t) = c_i E_i - i\hbar \sum_j c_j \dot{\mathbf{R}}(t)\cdot\mathbf{d}_{ij}, \tag{10}$$

where E_i is the energy of adiabatic state i, $\dot{\mathbf{R}}(t)$ contains the nuclear velocities, and $\mathbf{d}_{ij}$ is the nonadiabatic coupling vector,

$$\mathbf{d}_{ij} = \langle \psi_i | \nabla_{\mathbf{R}} | \psi_j \rangle, \tag{11}$$

which enters Eq. (10) by application of the chain rule

$$\langle \psi_i | \partial/\partial t | \psi_j \rangle = \dot{\mathbf{R}}(t)\cdot\mathbf{d}_{ij}. \tag{12}$$

Methods for evaluating the nonadiabatic couplings given by the $\mathbf{d}_{ij}$ are discussed in Section 4.3. The matrix elements of the nuclear kinetic energy operator $\hat{T}(\mathbf{R})$ probe second derivatives of the electronic wave function with respect to the nuclear coordinates. These are small compared to the $\mathbf{d}_{ij}$ and are usually neglected [57–59].

In surface-hopping methods classical trajectories evolve under the forces determined from a single quantum state k,

$$\mathbf{F}_{\mathrm{SH}} = -\left\langle \psi_k \middle| \nabla_{\mathbf{R}} \hat{H}_0(\mathbf{R}) \middle| \psi_k \right\rangle. \tag{13}$$

At various points along the trajectory, generally coinciding with regions of strong interstate coupling, hops may take place to different states to reflect the cumulative occupation probabilities determined by the $|c_i(t)|^2$. The force on a surface-hopping trajectory responds to changes in the total quantum wave function only at the points where hops can occur. Self-consistency between the quantum wave function and the classical degrees of freedom is thus not realized on an individual trajectory, but is realized for the ensemble of trajectories, which maintains the correct population of quantum states.

Tully has introduced a general and easily applied SH method called molecular dynamics with quantum transitions (MDQT) [60,61]. Coker and co-workers have discussed this method extensively and made numerous applications to multidimensional systems of physical and experimental interest [21,59,62–64]. In MDQT, the quantum amplitudes (Eq. (10)) are integrated throughout the course of a trajectory. At every time step a decision is made whether to switch to a new state using a ''fewest switches'' algorithm designed to minimize the total number of hops [59,60]. This algorithm correctly reproduces the probabilities $|c_i(t)|^2$ of occupying each quantum state at any time along a given trajectory. Two major advantages of MDQT over previous SH methods [57,58] are that regions of strong coupling do not have to be identified in advance and regions of extended coupling may be treated. Both of these properties make MDQT easy to implement in any system, regardless of size, as long as the necessary potential surfaces and couplings can be computed at arbitrary configurations.

A source of concern in obtaining accurate results from MDQT trajectories is the length of time the quantum mixed state used to determine surface hopping is allowed to propagate before being resolved. In the original presentation of the method quantum phase coherence was maintained for all time. This gives rise to two problems: spurious interference effects may arise from multiple passages through regions of strong nonadiabatic coupling, and the nonadiabatic transition rates themselves may be incorrect. Some method of determining an appropriate ''decoherence time'' and resolving the mixed quantum state on this time scale must therefore be devised. Building on work by Nitzan and co-workers [65,66], Rossky and co-workers [67–69] have developed a practical scheme for estimating decoherence times in multidimensional systems. The key quantity in their analysis is the overlap $J(t)$ between the nuclear wave functions propagated for time t on the two different potential surfaces,

$$J(t)=\left\langle \chi(\mathbf{R}(0)) \right| e^{iH_2 t/\hbar} e^{-iH_1 t/\hbar} \left| \chi(\mathbf{R}(0)) \right\rangle. \tag{14}$$

Decay of the nuclear overlap places an upper bound on the time scale for the loss of quantum coherence in nonadiabatic transitions, and has been used to define the characteristic decoherence time [67–69]. The loss of quantum coherence signaled by the decay of the nuclear overlap can be quantified by making a Frozen Gaussian approximation [70] to evaluate the nuclear wave functions [67–69]. By averaging $J(t)$ over an ensemble of photodissociation trajectories, we have found that for $I_2^-Ar_n$ clusters the decoherence time is on the order of several hundred fs.

The algorithm used in this work to compute surface-hopping closely follows the MDQT prescription of Tully [60,61], modified to account for the quantum decoherence. At the beginning of a trajectory the quantum amplitudes are initialized with the amplitude of the initially occupied state set to one and all others set to zero. At each time step, the classical equations of motion are propagated forward one classical time step, Δ. The equations for quantum amplitudes (Eq. (10)) are then integrated on this interval using an adaptive time step that is much smaller than Δ to ensure convergence of the amplitudes. Values of the adiabatic energies and the nonadiabatic couplings are obtained along the interval through linear interpolation using the values from the classical trajectory computed at the endpoints of the interval. The classical time step must be small enough that the adiabatic energies and couplings vary smoothly on the interval, so that interpolation of their values is accurate. The nonadiabatic couplings may be computed exactly at the interval endpoints, but we have chosen to follow the prescription of Tully and Hammes-Schiffer [61] and compute $[\dot{\mathbf{R}}\cdot\mathbf{d}_{ij}](t+\Delta/2)$ by a symmetrized finite difference. The values at $t-\Delta/2$ are saved and linear interpolation and extrapolation are used to compute values intermediate between t and $t+\Delta$. The overlap of the quantum eigenvectors at successive classical steps is required to meet a threshold (usually 0.9) in order to ensure that narrow regions of strong coupling are not missed by the integration. The classical stepsize is adaptively reduced when the overlap falls below threshold.

Our implementation of surface hopping collapses the quantum amplitudes onto a single state periodically during the course of a trajectory to mitigate the effects of spurious quantum coherence. The mixed state is resolved into its eigenstates by setting $c_k=1$ for the occupied state and all other amplitudes to zero. It is important that this not be done when the trajectory is in a region of strong nonadiabatic coupling because this can cause serious errors in the hopping probabilities, particularly in regions with weakly avoided crossings. In this work amplitude resetting was attempted at 100 fs intervals along each trajectory, and amplitudes were reset only if the magnitude of each nonadiabatic coupling element $\dot{\mathbf{R}}(t)\cdot\mathbf{d}_{ij}$ arising from the currently occupied state fell below a threshold of 10^{-5} atomic units. This procedure does not damp coherence that arises in extended coupling regions, but prevents coherence from arising on separate passages through strong coupling regions.

Tully's ''fewest switches'' algorithm determines surface hopping from the probability flux rather than the amplitudes themselves. The change in probability per unit time of occupying state k is given by [60]

$$\dot{\rho}_{kk}=-\sum_j 2\mathrm{Re}\left[c_j c_k^*\left(\mathbf{R}\cdot\mathbf{d}_{kj}\right)\right]\equiv\sum_{j\neq k} b_{kj}, \tag{15}$$

so the probability flux out of state k into state j per unit time is $-b_{kj}$. Over a finite time interval Δt, the probability of making a hop from state k to state j is

$$g_{kj} = \frac{-\int_t^{t+\Delta t} b_{kj}(t')\,dt'}{\rho_{kk}(t)}, \tag{16}$$

where $\rho_{kk}(t)$ is the probability of occupying state k at time t. These transition probabilities can be integrated along with the quantum amplitudes at little extra expense. At the end of each classical time step, the transition probabilities are used to determine whether hops take place based on comparison with a random number $0 < \zeta < 1$. A hop can take place to state j only if $g_{kj} > 0$ and $\zeta < g_{kj}$. The number of hops between states is minimized by this first criterion that $g_{kj} > 0$, which means that hops take place only when there is a net flux of probability into the target state. If multiple g_{kj} are greater than zero, hops are determined by considering the target states in succession, subtracting g_{kj} from ζ for each state to which no hop occurs. If no hop is made to any state, integration of the trajectory continues on the current state k.

When the algorithm determines that a hop should occur, the velocities must be adjusted to conserve energy in the new state. The MDQT procedure calls for scaling the velocities by applying an instantaneous force in the direction $\mathrm{Re}[\mathbf{d}_{kj}]$. Scaling the velocities subject to a set of arbitrary constraints on the velocities in the system requires determining a single scale factor γ, where the velocities for each atom i are changed according to

$$\mathbf{v}_i^{\text{new}}(\gamma) = \mathbf{v}_i^{\text{old}} + \frac{\gamma}{m_i}\mathrm{Re}\left[\mathbf{d}_{kj}^{(i)}\right]. \tag{17}$$

The molecular constraints are applied to $\mathbf{v}^{\text{new}}(\gamma)$ using the methods described in Section 4.1 above. When the target state is higher in energy than the current state, the kinetic energy may not be large enough to compensate for the change in potential energy, i.e. the transition may be classically forbidden. In this case the hop is rejected and the current state is not changed. The MDQT procedure also specifies that the component of the velocity in the direction of the nonadiabatic coupling be reversed [61]. In practice, tests on photodissociation in $I_2^- Ar_n$ clusters seem to indicate that performing the reversal has little effect on the branching ratios [23] but does have the undesirable effect of introducing instantaneous dephasing of the solute vibrations. This effect has also been noted by Müller and Stock [71], who have suggested dropping this procedure from the MDQT algorithm, and this has been done in the simulations described here.

4.3. Forces and nonadiabatic couplings

Computing MD trajectories and surface-hopping requires determination of forces on the adiabatic potentials and nonadiabatic couplings between the potential surfaces. Since this is generally the most time-consuming part of any simulation it requires careful consideration. In the following subsections we discuss our general procedure for evaluating these forces and nonadiabatic couplings, present a prescription for matching the phases of the complex eigenvectors (required for the current problem because of the Kramers degeneracy resulting from unpaired electron spins), and finally give explicit formulas for evaluating the derivatives of the model Hamiltonian.

4.3.1. General formulas

If we assume that the adiabatic states, ψ_k are defined in terms of an orthonormal set of functions, ϕ_n, such that

$$|\psi_k\rangle = \sum_n \Gamma_{nk} |\phi_n\rangle, \tag{18}$$

then the Hellmann-Feynman [72] theorem gives the forces on state k

$$\mathbf{F}_k = -\nabla_{\mathbf{R}}\langle\psi_k|\hat{H}|\psi_k\rangle = -\langle\psi_k|\nabla_{\mathbf{R}}\hat{H}|\psi_k\rangle. \tag{19}$$

The important point here is that calculating the forces requires only derivatives of the Hamiltonian and not the derivatives of the eigenfunctions, which are more complicated to compute. The nonadiabatic couplings are given by an off-diagonal version of this relation [58,73,74]

$$\mathbf{d}_{jk} = \frac{\langle\psi_j|\nabla_{\mathbf{R}} H|\psi_k\rangle}{E_k - E_j} + \sum_{nn'} \Gamma_{nk}^* \Gamma_{n'j} \langle\phi_n|\nabla_{\mathbf{R}}\phi_{n'}\rangle, \tag{20}$$

which involves derivatives of the basis functions with respect to the classical coordinates,

$$\mathbf{D}_{nn'} = \langle \phi_n | \nabla_{\mathbf{R}} \phi_{n'} \rangle, \tag{21}$$

but not of the coefficients that define the adiabatic states. This is useful because obtaining the derivatives of the eigenvector coefficients is a much more involved process than obtaining the eigenvectors themselves, which is done using canned matrix diagonalization routines. For the low-lying electronic states of I_2^-, the $\mathbf{D}_{nn'}$ vanish by symmetry. For other molecules, such as ICl^-, this is not the case and the basis function derivatives are evaluated using finite difference approximations [27]. The full nonadiabatic coupling vector is required by the MDQT method only when hops occur; at other times the couplings required to integrate the quantum amplitudes (Eq. (10)) can be computed by a simple finite difference scheme [27,61].

4.3.2. Phase matching of eigenvectors

In the open-shelled molecules studied in this work the presence of unpaired electrons gives rise to state degeneracies that are not lifted by any electrostatic interactions with the solvent. Numerical determination of these degenerate eigenstates results in an arbitrary phase being associated with each of the degenerate eigenvectors. If this phase is not preserved in calculations at neighboring geometries, the nonadiabatic coupling calculated from these states will oscillate wildly, making numerical integration of the quantum amplitudes impossible. Several methods of handling this problem have been suggested [16,75–78]; we have adopted the procedure of Maslen et al. [16]. The eigenvectors determined by this method of phase matching have been tested numerically by comparing values of the nonadiabatic couplings computed analytically using Eq. (20) with couplings computed using finite differences; the good agreement shows that the phase matching scheme adopted here is adequate for computing nonadiabatic dynamics on these potential surfaces.

Our phase matching prescription requires that the nonadiabatic couplings vanish for each member of the degenerate manifold

$$\langle \psi_j | \partial / \partial t | \psi_k \rangle = 0, \quad \forall j,k \in K, \tag{22}$$

where K denotes the indices of the manifold members. This requirement can be written in matrix notation as

$$\mathbf{\Gamma}_K^\dagger(t)\dot{\mathbf{\Gamma}}_K(t) + \mathbf{\Gamma}_K^\dagger(t)(\dot{\mathbf{R}} \cdot \mathbf{D})\mathbf{\Gamma}_K(t) = 0, \tag{23}$$

where $\mathbf{\Gamma}_K(t)$ is a matrix whose columns contains the manifold eigenvectors. Using a finite difference approximation to the time derivative this equation can be manipulated to give

$$\mathbf{\Gamma}_K(t+\Delta) = [\mathbf{1} - \delta\mathbf{R} \cdot \mathbf{D}]\mathbf{\Gamma}_K(t), \tag{24}$$

where $\delta\mathbf{R} = \mathbf{R}(t+\Delta) - \mathbf{R}(t)$. Now if $\mathbf{\Gamma}_K'(t+\Delta)$ contains the eigenvectors obtained from numerical diagonalization of the Hamiltonian, the phase-matched eigenvectors at the new time are related to these unmatched eigenvectors by the unitary transformation

$$\mathbf{\Gamma}_K'(t+\Delta) = \mathbf{\Gamma}_K(t+\Delta)\mathbf{U}. \tag{25}$$

Putting this into the phase matching requirement given by Eq. (24) gives the desired transformation matrix

$$\mathbf{U} = \mathbf{\Gamma}_K^\dagger(t)[\mathbf{1} + \delta\mathbf{R} \cdot \mathbf{D}]\mathbf{\Gamma}_K'(t+\Delta). \tag{26}$$

$\mathbf{U}$ is only unitary in the limit of an infinitesimal time step, so to maintain the orthonormality of the phase matched eigenvectors, $\mathbf{U}$ is transformed using symmetric orthogonalization.

4.3.3. Derivatives of the model Hamiltonian

In Section 3 we presented an effective Hamiltonian for clusters including the electronic states of the solute and the interactions among solute and solvent molecules. We now discuss the computation of the analytic derivatives of this Hamiltonian that are needed to determine the forces and nonadiabatic couplings. The discussion includes only the derivatives of the electrostatic terms, since derivatives of the remaining pairwise terms are standard quantities in MD simulations and have been discussed extensively elsewhere [51,79]. The derivatives of the electrostatic terms are expressed in Stone's notation [22,35] as forces and torques acting on the individual multipole sites. The procedures for converting these forces and torques into forces on the primary atoms, as required by our method of computing the molecular dynamics, are described following discussion of the basic derivatives.

The effective Hamiltonian for the electrostatic and polarization interactions of the solute and solvent can be expanded into five terms,

$$\hat{h}^{\mathrm{lr}} = \tfrac{1}{2} Q \cdot T \cdot Q + \hat{q} \cdot T \cdot Q - \tfrac{1}{2} Q \cdot T \cdot \boldsymbol{\chi} \cdot T \cdot Q - \hat{q} \cdot T \cdot \boldsymbol{\chi} \cdot T \cdot Q - \tfrac{1}{2} \hat{q} \cdot T \cdot \boldsymbol{\chi} \cdot T \cdot \hat{q}, \tag{27}$$

where the first two terms contain the interactions among the permanent multipoles and the last three terms contain the interactions of the permanent multipoles with the induced moments. It is convenient to discuss the derivatives arising from each of these interactions separately because of the large number of terms that arise. The derivatives are computed in terms of the generalized coordinate X_i, which represents the Cartesian and angular coordinates of each of the multipole sites in the system.

The forces due to the first term in Eq. (27), the interactions of the permanent solvent multipoles, are given by

$$F_i^{(1)} = -\tfrac{1}{2} \frac{\partial}{\partial X_i} (Q \cdot T \cdot Q) = -\tfrac{1}{2} Q \cdot \frac{\partial T}{\partial X_i} \cdot Q, \tag{28}$$

where we have assumed for simplicity that the multipoles contained in Q do not depend on any of the coordinates X_i. Because this term does not depend on the electronic state of the solute, it contributes the same to all of the adiabatic forces and does not contribute to the nonadiabatic couplings. Computation of the forces from this equation and the similar but more complicated expressions presented below may be performed very efficiently. The tensor T contains only pairwise interactions so that there are at most 12 nonzero derivatives of each element T_{ab}, because each multipole site is defined by three position and three orientation coordinates. In fact, since $\mathbf{F}_a = -\mathbf{F}_b$, there are at most 9 unique derivatives. As we will see below, computation of these derivatives involves simple terms already required for the evaluation of the energy, and calculation of the adiabatic energies and forces is only about three times as expensive as calculation of the energies alone.

Terms involving the solute multipole operators $\hat{q}$ depend on the solute electronic state. The matrix elements of the derivatives of the second term in Eq. (27), the interactions of the solute multipole operators with the permanent solvent multipoles, are given by

$$\left(d_{jk}^{(2)} \right)_i = \left\langle \phi_j \middle| \frac{\partial}{\partial X_i} \hat{q} \cdot T \cdot Q \middle| \phi_k \right\rangle = q_{jk} \cdot \frac{\partial T}{\partial X_i} \cdot Q + \frac{\partial R_c}{\partial X_i} \left(\frac{\partial q_{jk}}{\partial R_c} \cdot T \cdot Q \right), \tag{29}$$

where $(d_{jk}^{(2)})_i$ refers to the matrix elements of the Hamiltonian derivatives rather than the nonadiabatic couplings, which are computed from these derivatives using Eq. (20). q_{jk} represents the matrix elements of the multipole operators, $\langle \phi_j | \hat{q} | \phi_k \rangle$. Derivatives of these operators with respect to the internal solute coordinate R_c are nonzero, and are determined, as are the multipole operators themselves, by cubic spline interpolation. It is in fact rare during the course of a trajectory that all of the derivative matrix elements are evaluated in this way—only when the full nonadiabatic coupling vector is required to adjust the classical velocities following a hop. The remainder of the time only the force on a given adiabatic state ψ is required:

$$\left(F_\psi^{(2)} \right)_i = \langle \hat{q} \rangle_\psi \cdot \frac{\partial T}{\partial X_i} \cdot Q + \frac{\partial R_c}{\partial X_i} \left(\frac{\partial \langle \hat{q} \rangle_\psi}{\partial R_c} \cdot T \cdot Q \right). \tag{30}$$

Because only the expectation value of $\hat{q}$ is needed, computation of the forces arising from the quantum wave function is only marginally more expensive than calculation of the purely classical forces.

The terms involving the induced moments can be evaluated by making use of the relation

$$\frac{\partial \boldsymbol{\chi}}{\partial X_i} = \frac{\partial [T + \boldsymbol{\alpha}^{-1}]^{-1}}{\partial X_i} = -[T + \boldsymbol{\alpha}^{-1}]^{-1} \cdot \frac{\partial T}{\partial X_i} \cdot [T + \boldsymbol{\alpha}^{-1}]^{-1} = -\boldsymbol{\chi} \cdot \frac{\partial T}{\partial X_i} \cdot \boldsymbol{\chi}. \tag{31}$$

The forces due to the third term in Eq. (27), the interactions of the permanent solvent multipoles with the induced multipoles, are given by

$$F_i^{(3)} = \tfrac{1}{2} \frac{\partial}{\partial X_i} (Q \cdot T \cdot \boldsymbol{\chi} \cdot T \cdot Q) = -Q \cdot \frac{\partial T}{\partial X_i} \cdot \boldsymbol{\Delta}_Q - \tfrac{1}{2} \boldsymbol{\Delta}_Q \cdot \frac{\partial T}{\partial X_i} \cdot \boldsymbol{\Delta}_Q, \tag{32}$$

which has been simplified by identifying the induced moments, $\mathbf{\Delta}_Q \equiv -\boldsymbol{\chi} \cdot T \cdot Q$. The matrix elements of the derivatives of the fourth term in Eq. (27), the cross term between the solute and solvent multipoles interacting with the induced moments are

$$\begin{aligned}\left(d_{jk}^{(4)}\right)_i &= \left\langle \phi_j \left| \frac{\partial}{\partial X_i}\left(-\hat{q} \cdot T \cdot \boldsymbol{\chi} \cdot T \cdot Q\right) \right| \phi_k \right\rangle \\ &= \frac{\partial R_c}{\partial X_i}\left(\frac{\partial q_{jk}}{\partial R_c} \cdot T \cdot \mathbf{\Delta}_Q\right) \\ &\quad + q_{jk} \cdot \frac{\partial T}{\partial X_i} \cdot \mathbf{\Delta}_Q + \mathbf{\Delta}_{jk} \cdot \frac{\partial T}{\partial X_i} \cdot \mathbf{\Delta}_Q \\ &\quad + \mathbf{\Delta}_{jk} \cdot \frac{\partial T}{\partial X_i} \cdot Q, \end{aligned} \tag{33}$$

where $\mathbf{\Delta}_{jk} \equiv -\boldsymbol{\chi} \cdot T \cdot q_{jk}$ are the induced moments due to the solute multipole matrix elements. It is also useful to express the forces arising from this term on the adiabatic state ψ,

$$\begin{aligned}\left(F_\psi^{(4)}\right)_i &= -\frac{\partial R_c}{\partial X_i}\left(\frac{\partial \langle \hat{q} \rangle_\psi}{\partial R_c} \cdot T \cdot \mathbf{\Delta}_Q\right) \\ &\quad - \langle \hat{q} \rangle_\psi \cdot \frac{\partial T}{\partial X_i} \cdot \mathbf{\Delta}_Q - \mathbf{\Delta}_\psi \cdot \frac{\partial T}{\partial X_i} \cdot \mathbf{\Delta}_Q \\ &\quad - \mathbf{\Delta}_\psi \cdot \frac{\partial T}{\partial X_i} \cdot Q, \end{aligned} \tag{34}$$

where $\mathbf{\Delta}_\psi \equiv -\boldsymbol{\chi} \cdot T \cdot \langle q \rangle_\psi$. The fifth and final term in Eq. (27), which arises from the interaction of the solute multipoles with the induced moments, is a two electron operator and is thus somewhat more complicated to evaluate. This operator is determined in terms of one electron operators by inserting the identity operator, $\hat{1} = \sum_n |\phi_n\rangle\langle\phi_n|$, which is approximated by restricting the sum to the basis set used in the calculation of the adiabatic states. The derivative matrix elements are then given by

$$\begin{aligned}\left(d_{jk}^{(5)}\right)_i &= \left\langle \phi_j \left| \frac{\partial}{\partial X_i}\left(-\tfrac{1}{2}\hat{q} \cdot T \cdot \boldsymbol{\chi} \cdot T \cdot \hat{q}\right) \right| \phi_k \right\rangle \\ &= \tfrac{1}{2}\sum_n \left\{ \frac{\partial R_c}{\partial X_i}\left(\frac{\partial q_{jn}}{\partial R_c} \cdot T \cdot \mathbf{\Delta}_{nk} + \frac{\partial q_{nk}}{\partial R_c} \cdot T \cdot \mathbf{\Delta}_{jn}\right) \right. \\ &\quad + q_{jn} \cdot \frac{\partial T}{\partial X_i} \cdot \mathbf{\Delta}_{nk} + q_{nk} \cdot \frac{\partial T}{\partial X_i} \cdot \mathbf{\Delta}_{jn} \\ &\quad \left. + \mathbf{\Delta}_{jn} \cdot \frac{\partial T}{\partial X_i} \cdot \mathbf{\Delta}_{nk} \right\}. \end{aligned} \tag{35}$$

The adiabatic forces arising from this term simplify to

$$\begin{aligned}\left(F_\psi^{(5)}\right)_i &= -\sum_n \left\{ \frac{\partial R_c}{\partial X_i} \mathrm{Re}\left(\frac{\partial q_{\psi n}}{\partial R_c} \cdot T \cdot \mathbf{\Delta}_{n\psi}\right) \right. \\ &\quad + \mathrm{Re}\left(q_{\psi n} \cdot T \cdot \mathbf{\Delta}_{n\psi}\right) \\ &\quad \left. + \tfrac{1}{2}\mathbf{\Delta}_{\psi n} \cdot \frac{\partial T}{\partial X_i} \cdot \mathbf{\Delta}_{n\psi} \right\}, \end{aligned} \tag{36}$$

where $q_{\psi n} \equiv \langle \psi | \hat{q} | \phi_n \rangle$ and $\mathbf{\Delta}_{n\psi} \equiv -\boldsymbol{\chi} \cdot T \cdot q_{n\psi}$. This completes the formulas required to compute the derivatives and forces for the effective Hamiltonian model. We have tested all of the forces and nonadiabatic couplings computed analytically using the above formulas against finite difference approximations to the same quantities to ensure that the expressions have been coded correctly.

To conclude, we briefly discuss evaluation of the derivatives of the interaction tensor matrix elements required to compute the forces. The tensor matrix elements derived by Stone and co-workers [35] are expressed in terms of 16 basic variables involving the multipole site positions and the axes used to define the multipoles. The interaction between two multipole sites a and b on molecules A and B is illustrated in Fig. 8. The fundamental quantities that

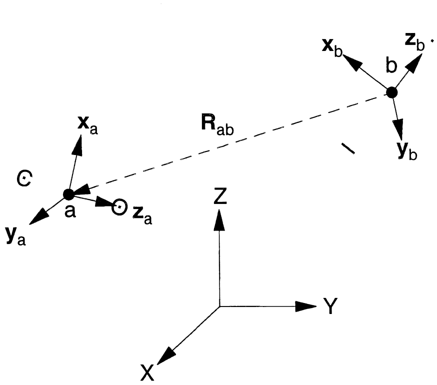

Fig. 8. Vectors describing the interaction of two multipole sites on different molecules. Vectors denoted by a capital letter are fixed in the space frame, while lowercase vectors are body-fixed.

occur in the tensor formulas are R_{ab}, the separation vector between sites a and b, and the multipole axes, $\mathbf{w}_a = \mathbf{x}_a, \mathbf{y}_a, \mathbf{z}_a$ and $\mathbf{w}_b = \mathbf{x}_b, \mathbf{y}_b, \mathbf{z}_b$. The axes defining the multipoles on each site may in general differ from the molecular axes, but they are taken to be the same in this work. The 16 variables that occur in the interaction tensor formulas are R_{ab}, $\mathbf{w}_a \cdot \mathbf{R}_{ab}$, $\mathbf{w}_b \cdot \mathbf{R}_{ab}$, and $\mathbf{w}_a \cdot \mathbf{w}_b$. So, for example, the tensor element between the z component of the dipole moment on site a and a charge on site b is given by

$$T_{10,00}^{ab} = \frac{-(\mathbf{z}_a \cdot \mathbf{R}_{ab})}{R_{ab}^3}. \tag{37}$$

In Stone's formulation, the derivatives of these tensor elements are converted to forces and torques acting on the molecular center-of-mass by making use of the chain rule and the derivatives of the 16 basic variables with respect the the center of mass position and orientation [35,80]. This assumes that the molecules are rigid, and the approach must be modified to apply to the nonrigid molecules, particularly the solute, considered by our method. We do this by converting the derivatives of the tensor elements with respect to the 16 fundamental variables to forces and torques acting on the multipole sites. These forces and torques are then converted to forces on the primary atoms following an additional application of the chain rule to determine the derivatives of the multipole positions and orientations with respect to the primary atom positions. The details of this analysis are given in Ref. [27].

5. Photodissociation, recombination and electronic relaxation in $I_2^-(CO_2)_n$ clusters

We have applied the methods described in preceding sections to I_2^- clustered with Ar [23,25], CO_2 [24] and OCS [10] and to ICl^- clustered with CO_2 [27,81]. We choose $I_2^-(CO_2)_n$ to illustrate the method as this system is the most extensively studied in the experiments. While some of our results have been described in an earlier communication [24], we focus here on the time scales for electronic transitions, a subject only briefly discussed in Ref. [24].

Two different ensembles, designed to emphasize different aspects of the dynamics, have been used in the simulations described here. The first ensemble includes 41 trajectories for each cluster size, integrated for up to 200 ps. The initial conditions were obtained by sampling a single 400 ps trajectory with an average temperature of 80 K. The products are determined by integrating the trajectories until the nuclear configuration meets either of two criteria: the I–I distance exceeds 20 Å, or I_2^- undergoes more than 100 oscillations in a particular potential well. The second type of ensemble consists of 200 trajectories, each of which is integrated for 10 ps. This ensemble was used to explore the short-time dynamics of electronic relaxation in clusters containing 9, 12, and 16 CO_2 molecules.

The comparison of simulated and experimental photoproduct distributions in Fig. 9(a) demonstrates the accuracy of the model. The product distributions agree to within the statistical errors in the simulation at all cluster sizes. Fig. 9(b) introduces a collective ‘‘solvent coordinate’’, $\Delta\Phi$, that measures the asymmetry of the electrostatic environment around the solute. $\Delta\Phi$ is defined as the change in energy when a charge of $-e$ is moved from I_A to I_B while holding the solute and solvent nuclear coordinates fixed. The figure shows the equilibrium ensemble average of $\Delta\Phi$ for clusters in their electronic ground state. The CO_2-CO_2 interactions are strong, so the solvent molecules cluster together, forming a cage around one end of the solute at $n = 9$ and closing a complete solvent shell at $n = 16$. Thus, in $I_2^-(CO_2)_9$ photodissociation begins from a highly asymmetric solvent configuration, whereas in $I_2^-(CO_2)_{16}$ the solvent is much more symmetric.

Fig. 10 shows the ensemble-averaged populations in each electronic state as a function of time as determined from the 200 trajectory/10 ps ensembles. The two repulsive curves are very close in energy and are strongly coupled to each other, so we have added their populations together and referred to the sum as the A' population. Also, we have removed from the average those trajectories that dissociate within 10 ps. Trajectories reach the X state by two pathways: roughly 25% hop directly from A' to X, while the remainder hop first to the A state. No trajectories dissociate directly on the A' state. The figure shows that electronic relaxation is characterized by more than one time scale; for example, in the case of $n = 16$, trajectories leave the A' state in 1–2

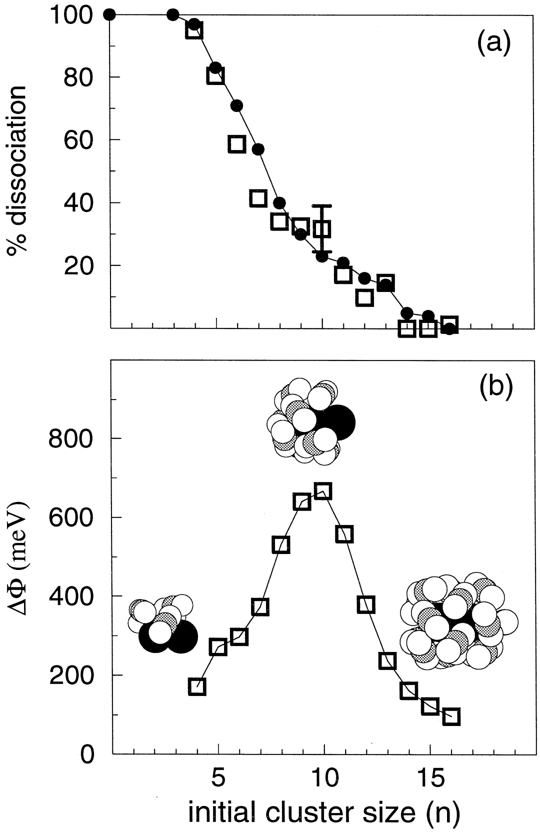

Fig. 9. (a) Branching ratio for the products of $I_2^-(CO_2)_n$ photodissociation at 790 nm. The filled circles are the experimental data and the squares show the simulation results. The 1σ error bar shown for $n=10$ is based on the statistical sampling and is representative of the error bars at other cluster sizes. (b) Ensemble average of the magnitude of the solvent coordinate as a function of cluster size. Typical structures for $n=5$, 10, and 16 are shown.

ps and the X state population rises to 50% by about 3 ps, after which there is a very slow relaxation from A to X. Eventually all of the A state molecules either relax or dissociate. As noted in Ref. [24], the I_2^- binding energy on the A state is only 100 meV, about half the binding energy of a single CO_2 molecule with I^-. The solvent thus tends to push apart the I_2^- bond and localize the excess charge. The resulting ''solvent-separated pair'', in which an I^- ion is weakly bound to several CO_2 molecules and one I atom, is shown in Fig. 11(b).

As the geometry of the hot cluster fluctuates, it passes through regions of strong coupling to the X state, where recombination can occur; alternatively, the solute may completely dissociate via evaporation of the neutral iodine. The decay of these meta-stable clusters accounts for the slow transfer of population from the A to the X state. We define an overall recombination time by

$$\tau = \int_0^\infty f(t)\,\mathrm{d}t, \tag{38}$$

where $f(t)$ is the fraction of trajectories that have not recombined at time t, including only those trajectories which ultimately recombine. From our 41 trajectory/200 ps ensembles we calculate τ to be 12.8, 10.1, and 17.1 ps for $n=9$, 12, and 16, respectively. This value is dominated by the slow A to X relaxation and strongly influenced by the few trajectories that have very long recombination times, upwards of 50 ps in some cases; for most purposes it is more informative to inspect Fig. 10 directly.

Perhaps the most surprising feature of this system is the remarkably high caging efficiency: simulation

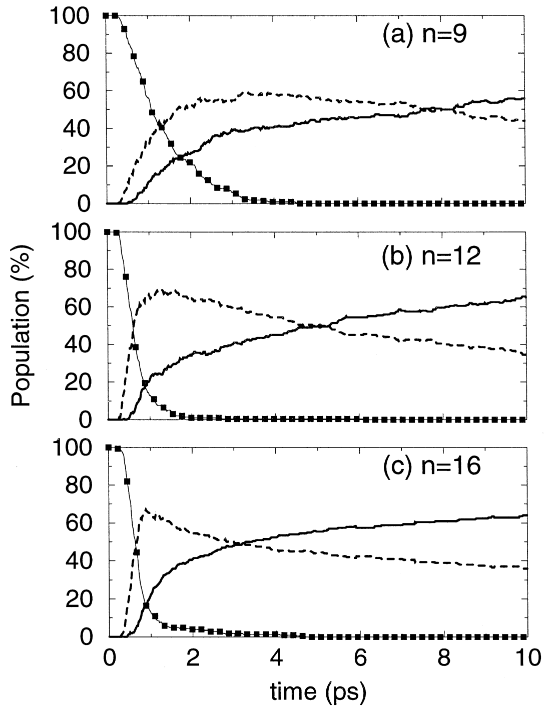

Fig. 10. Ensemble average of the population of each solute electronic state versus time for $I_2^-(CO_2)_n$. The A' state curve is marked with squares, dotted and solid lines correspond to the A and X states, respectively.

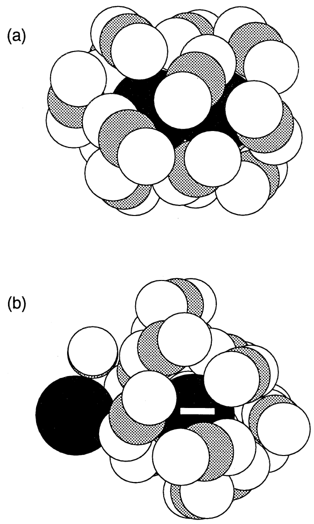

Fig. 11. Typical configurations for $I_2^-(CO_2)_{16}$. (a) At equilibrium on the X state. (b) A solvent-separated pair on the A state.

and experiment both show significant recombination for clusters having as few as 5 CO_2 molecules, less than one third of a solvent shell. Related to this is our observation that dissociation never takes place on the initially excited A' state. We explain these results in terms of the polarization of the charge distribution on the solute by the solvent. In the electronic ground state, and in excited states that are primarily bonding in character, an asymmetric solvent environment causes the solute charge to flow towards the more favorably solvated I atom. In antibonding excited states, however, the charge moves in the opposite direction. This counterintuitive behavior, which we have called ''anomalous charge switching'' [16,17], may be understood in terms of a simple diatomic LCAO-MO picture. In the isolated molecule the atomic orbitals combine into bonding and antibonding molecular orbitals, both of which are delocalized. An asymmetric solvent environment polarizes the solute charge distribution to an extent that depends on the strength of the solute-solvent interaction relative to the bonding interaction. The bonding molecular orbital becomes distorted so that most of the wave function amplitude resides on the more solvated atom, and since the ground and excited states must remain orthogonal, the antibonding MO must polarize in the opposite direction. Thus charge flows towards the solvent in the ground state, and away from the solvent in the excited state. In other words, in an antibonding state the component of the molecular polarizability tensor parallel to the internuclear axis is negative.

In real molecules, the magnitude and direction of charge flow depends on the details of the solute electronic structure, which in the halogens is affected by strong spin-orbit coupling. From our electronic structure calculations we find that the X and A states show normal charge flow, while the A' state shows anomalous charge flow at most internuclear distances. (In the immediate vicinity of the Franck-Condon region, charge flow on the A' state is normal, but trajectories leave this region too quickly for this to influence their dynamics.) Dissociation in the A' state thus requires ejection of an ion from the cluster. The nascent ion is held back by the electrostatic and polarization interactions with the neutral cluster that it is trying to escape, and in CO_2 clusters these forces are strong enough to suppress the direct dissociation pathway even in very small clusters. This contrasts with the more weakly bound Ar clusters, in which direct dissociation on the A' state is observed in the simulations, providing a likely explanation for the experimentally observed bimodal mass distribution in the dissociation products [23].

The contrast between anomalous charge flow on the A' state and normal charge flow on the A and X states also plays a key role in the electronic relaxation at short times. Fig. 12 shows the ensemble average of $|\Delta\Phi|$ during the first 2 ps after excitation.

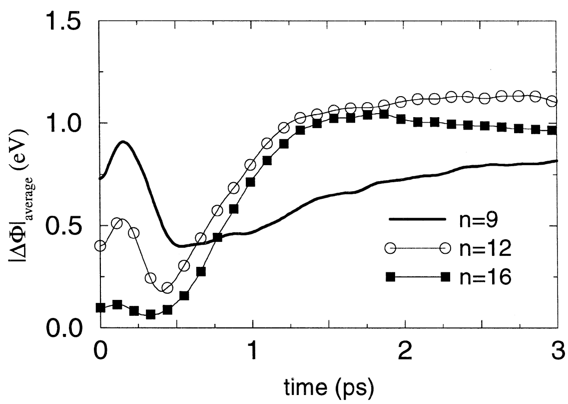

Fig. 12. Ensemble average of the magnitude of the solvent coordinate versus time for $n = 9$, 12, and 16. The rise at 500 fs is evidence of solvent rearrangement following electronic relaxation.

As the equilibrium geometries in Fig. 9(b) illustrate, $I_2^-(CO_2)_9$ starts out from a much more asymmetric solvent geometry than $I_2^-(CO_2)_{16}$. The initial rise in the solvent asymmetry at about 200 fs arises from solute, not solvent, motion: the iodine atom that was initially less solvated moves away from the cluster of solvent molecules, so that $\Delta\Phi$ increases. After this, however, the escaping charge draws the solvent towards a more symmetric configuration, as illustrated by the sample trajectory shown in Fig. 13. This is characteristic of anomalous-state solvent dynamics —because the charge and the solvent move in opposition to each other, the energy minimum occurs at $\Delta\Phi = 0$. Nonadiabatic coupling to the A and X states becomes important at bond lengths of 5–7 Å and small values of $\Delta\Phi$, as shown by the central dark circle in Fig. 13. Because the nonadiabatic coupling is confined to symmetric solvent geometries, trajectories beginning from initially symmetric solvent configurations undergo nonadiabatic transitions to the A and X states at earlier times than those starting from asymmetric configurations. As shown in Fig. 10, the decay rate of the A' state population following photoexcitation increases as the cluster size is increased from 9 to 16 because the initial configurations become more symmetric.

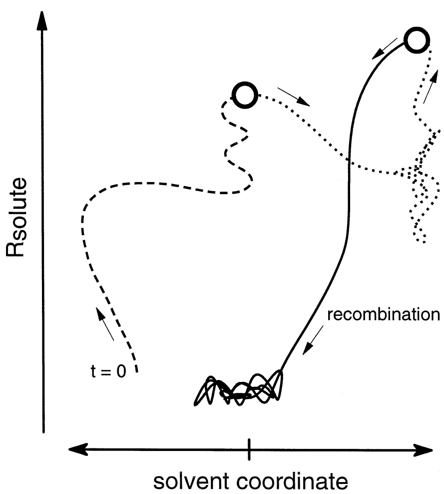

Fig. 13. Schematic diagram of recombination following photodissociation from an asymmetric cluster configuration. Dashed line: initial dissociation on the A' state; dotted line: temporary trapping on the A state; sold line: recombination on the X state. Circles mark the location of surface hopping events.

The transition from anomalous charge switching on the A' state to normal charge switching on the A or X states leads to a rapid increase in solvent asymmetry following the initial hop. At these longer bond lengths, the charge tends to localize on a single iodine atom, and because the solvent and the charge flow now act in concert, the solvent rearranges to stabilize the atomic ion, forming the solvent-separated pair mentioned earlier. The ion-solvent interactions are substantially larger than the A state potential well, so even though I_2^- separations characteristic of bound A-state I_2^- in the gas phase are observed, trajectories trapped in the A state always undergo transitions to the X state on a picosecond time scale. (In contrast, metastable $I_2^- Ar_n$ clusters in the A state have experimental lifetimes exceeding several microseconds [7].) Transitions from the A to X state require reorientation of the p orbital hole on the iodine atom and generally occur at somewhat longer bond lengths of 7–9 Å, where the solute electronic coupling is weak. The time scale on which these transitions occur appears to be governed by essentially diffusive motion along the I_2^- bond coordinate, as shown in Fig. 13. Hops to the X state may be followed by diffusive motion at long bond lengths, and hops back to the A state are possible. However once the solute bond length is significantly less than 6 Å on the X state, the strong bonding interactions in the ground state lead to rapid recombination and vibrational relaxation of I_2^-, as Fig. 13 illustrates.

A major goal of these simulations has been to provide an interpretation of the picosecond pump-probe absorption experiments of Lineberger and coworkers [5,8]. It is difficult to obtain a detailed picture of the photodissociation dynamics from these experiments alone because the absorption spectrum of I_2^- away from the equilibrium geometry is not known, and because the solvent may strongly affect the spectrum at these geometries. Simulation of the transient absorption spectrum from the trajectories, currently underway, will be required to make a direct comparison between the simulations and the experiments; however, it is possible to discuss the general features evident in both. The experiments suggest a time scale of about 20 ps for the overall process of electronic and vibrational relaxation in $I_2^-(CO_2)_9$, decreasing to about 10 ps for $n = 16$ [5,8]. The time scales generally agree with the time scales for electronic relaxation observed in the simulations, 10–20 ps, although the total relaxation time seems to be longer in the simulations at $n=16$ than in $n=9$. Both our simulations and previous theoretical investigations of I_2^- vibrational relaxation in the ground electronic state [17,20] have found that the time scale for vibrational relaxation is very fast (1–2 ps) in comparison to the electronic relaxation times found here. Furthermore, our simulations indicate that the rate of vibrational relaxation—even near the bottom of the potential well—does not vary substantially with cluster size in CO_2 clusters. It is thus likely, as Papanikolas et al. [17] have conjectured, that the time scale for electronic relaxation is the major contributor to the overall probe absorption recovery signal.

A major finding of the Lineberger experiments was the appearance of a ''bump'' centered at around 2 ps in the absorption recovery for $n \geq 14$ [5]. This bump, which has also been observed by Barbara and co-workers in both polar and nonpolar solutions [12–15], has been attributed to absorption from the inner turning point on A state following coherent recoil off the solvent cage. In the present simulations, motion along the I_2^- bond coordinate following electronic relaxation to the A state is diffusive, and a coherent return to short bond lengths in the excited state seems unlikely. As we have seen, the localization of charge on a single atom and the subsequent rearrangement of the solvent tends to keep the solute bond length large at short times. It is possible that the absorption bump arises from recoil in a small fraction of the ensemble that then absorbs strongly, but the simulations suggest other possibilities that should be investigated. In particular, more than a quarter of the trajectories hop directly from the A' state to the X state and recombine within 1–3 ps. While the experiments of Barbara and co-workers in solution appear to rule out the possibility that the transient feature arises from absorption at the bottom of the ground state well, the simulations show that strong absorption is possible at bond lengths of about 5 Å near the top of the ground state well. The passage of a substantial fraction of the directly recombining trajectories through this region could give rise to an observable transient absorption.

These simulations show that the model is capable of reproducing the experimental product distributions, and illustrate how the electronic properties of the excited states and their interactions with the solvent drive the dynamics of photodissociation in clusters. Further investigations, including direct simulation of the pump-probe spectrum spectrum, are needed to resolve more detailed questions such as the origin of the 2-ps feature in the transient absorption. These investigations are currently in progress and will be discussed in future publications.

Acknowledgements

We would like to John Papanikolas and Carl Lineberger for many helpful discussions. This work was supported by the National Science Foundation under Grants CHE-9217693 and PHY-9012244, and by the National Center for Supercomputing Applications (NCSA) under Grant CHE970015N for computing time on the Silicon Graphics Power ChallengeArray at the NCSA, University of Illinois at Urbana-Champaign.

References

[1] M. Alexander, N. Levinger, M. Johnson, D. Ray, W. Lineberger, J. Chem. Phys. 88 (1988) 6200.
[2] D. Ray, N. Levinger, J. Papanikolas, W. Lineberger, J. Chem. Phys. 91 (1989) 6533.
[3] J. Papanikolas, J. Gord, N. Levinger, D. Ray, V. Vorsa, W. Lineberger, J. Phys. Chem. 95 (1991) 8028.
[4] J. Papanikolas, V. Vorsa, M. Nadal, P. Campagnola, J. Gord, W. Lineberger, J. Chem. Phys. 97 (1992) 7002.
[5] J. Papanikolas, V. Vorsa, M. Nadal, P. Campagnola, H. Buchenau, W. Lineberger, J. Chem. Phys. 99 (1993) 8733.
[6] M.E. Nadal, P.D. Kleiber, W.C. Lineberger, J. Chem. Phys. 105 (1996) 504.
[7] V. Vorsa, P.J. Campagnola, S. Nandi, M. Larsson, W.C. Lineberger, J. Chem. Phys. 105 (1996) 2298.
[8] V. Vorsa, S. Nandi, P.J. Campagnola, M. Larsson, W.C. Lineberger, J. Chem. Phys. 106 (1997) 1402.
[9] A. Sanov, S. Nandi, W.C. Lineberger, J. Chem. Phys. 108 (1998) 5155.
[10] S. Nandi, A. Sanov, N. Delaney, J. Faeder, R. Parson, W.C. Lineberger, J. Phys. Chem. A, in press.
[11] M.E. Nadal, S. Nandi, D.W. Boo, W.C. Lineberger, in preparation.
[12] A.E. Johnson, N.E. Levinger, P.F. Barbara, J. Phys. Chem. 96 (1992) 7841.

[13] D.A.V. Kliner, J.C. Alfano, P.F. Barbara, J. Chem. Phys. 98 (1993) 5375.
[14] J. Alfano, Y. Kimura, P. Walhout, P. Barbara, Chem. Phys. 175 (1993) 147.
[15] P.K. Walhout, J.C. Alfano, K.A.M. Thakur, P.F. Barbara, J. Phys. Chem. 99 (1995) 7568.
[16] P.E. Maslen, J.M. Papanikolas, J. Faeder, R. Parson, S.V. ONeil, J. Chem. Phys. 101 (1994) 5731.
[17] J.M. Papanikolas, P.E. Maslen, R. Parson, J. Chem. Phys. 102 (1995) 2452.
[18] B.J. Gertner, K. Ando, R. Bianco, J.T. Hynes, Chem. Phys. 183 (1994) 309.
[19] R. Bianco, J.T. Hynes, J. Chem. Phys. 102 (1995) 7885.
[20] I. Benjamin, P.F. Barbara, B.J. Gertner, J.T. Hynes, J. Phys. Chem. 99 (1995) 7557.
[21] V.S. Batista, D.F. Coker, J. Chem. Phys. 106 (1997) 7102.
[22] A.J. Stone, The Theory of Intermolecular Forces, Oxford, New York, 1996.
[23] J. Faeder, N. Delaney, P. Maslen, R. Parson, Chem. Phys. Lett. 270 (1997) 196.
[24] N. Delaney, J. Faeder, P.E. Maslen, R. Parson, J. Phys. Chem. A 101 (1997) 8147.
[25] J. Faeder, R. Parson, J. Chem. Phys. 108 (1998) 3909.
[26] P.E. Maslen, J. Faeder, R. Parson, Mol. Phys. 94 (1998) 693.
[27] J. Faeder, PhD thesis, University of Colorado, 1998.
[28] P.E. Maslen, J. Faeder, R. Parson, Chem. Phys. Lett. 263 (1996) 63.
[29] MOLPRO, a package of ab initio programs by H.-J. Werner, P.J. Knowles, with contributions from J. Almlöf, R.D. Amos, M.J.O. Deegan, S.T. Elbert, C. Hampel, W. Meyer, K. Peterson, R. Pitzer, A.J. Stone, P.R. Taylor, version 94.3 (1994).
[30] M.T. Zanni, T.R. Taylor, B.J. Greenblatt, B. Soep, D.M. Neumark, J. Chem. Phys. 107 (1997) 7613.
[31] J.G. Dojahn, E.C.M. Chen, W.E. Wentworth, J. Phys. Chem. 100 (1996) 9649.
[32] E.C.M. Chen, J.G. Dojahn, W.E. Wentworth, J. Phys. Chem. A 101 (1997) 3088.
[33] A.J. Stone, Chem. Phys. Lett. 83 (1981) 233.
[34] A.J. Stone, M. Alderton, Mol. Phys. 56 (1985) 1047.
[35] S.L. Price, A.J. Stone, M. Alderton, Mol. Phys. 52 (1984) 987.
[36] C.S. Murthy, S.F. O'Shea, I.R. McDonald, Mol. Phys. 50 (1983) 531.
[37] M.J. Weida, D.J. Nesbitt, J. Chem. Phys. 105 (1996) 10210.
[38] A.J. Stone, R.J.A. Tough, Chem. Phys. Lett. 110 (1984) 123.
[39] B.T. Thole, Chem. Phys. 59 (1981) 341.
[40] Y. Zhao, C.C. Arnold, D.M. Neumark, J. Chem. Soc. Faraday Trans. 89 (1993) 1449.
[41] Y. Zhao, I. Yourshaw, G. Reiser, C.C. Arnold, D.M. Neumark, J. Chem. Phys. 101 (1994) 6538.
[42] I. Yourshaw, Y. Zhao, D.M. Neumark, J. Chem. Phys. 105 (1996) 351.
[43] D.W. Arnold, S.E. Bradforth, E.H. Kim, D.M. Neumark, J. Chem. Phys. 102 (1995) 3493.
[44] B.M. Ladanyi, R. Parson, J. Chem. Phys. 107 (1997) 9326.
[45] J.-P. Ryckaert, G. Ciccotti, H.J.C. Berendsen, J. Comput. Phys. 23 (1977) 327.
[46] W.F. van Gunsteren, H.J.C. Berendsen, Mol. Phys. 34 (1977) 1311.
[47] G. Ciccotti, M. Ferrario, J.-P. Ryckaert, Mol. Phys. 47 (1982) 1253.
[48] G. Ciccotti, J.-P. Ryckaert, Comput. Phys. Rep. 4 (1986) 345.
[49] L. Verlet, Phys. Rev. 159 (1967) 98.
[50] H.C. Andersen, J. Comput. Phys. 52 (1982) 24.
[51] M.P. Allen, D.J. Tildesley, Computer Simulation of Liquids, Clarendon Press, Oxford, 1987.
[52] R.S. Berry, Structure and dynamics of clusters: An introduction, in: G. Scoles (Ed.), The Chemical Physics of Atomic and Molecular Clusters, Proceedings of the International School of Physics Enrico Fermi, North-Holland, New York, 1990.
[53] W.H. Press, S.A. Teukolsky, W.T. Vetterling, B.P. Flannery, Numerical Recipes in C: The Art of Scientific Computing, Cambridge University Press, New York, 2nd edition, 1992.
[54] D. Lu, M. Zhao, D.G. Truhlar, J. Comp. Chem. 12 (1991) 377.
[55] L. Perera, F.G. Amar, J. Chem. Phys. 90 (1989) 7354.
[56] F.G. Amar, L. Perera, Z. Phys. D 20 (1991) 173.
[57] J.C. Tully, R.K. Preston, J. Chem. Phys. 55 (1971) 562.
[58] J.C. Tully, Nonadiabatic processes in molecular collisions, in: W.H. Miller (Ed.), Dynamics of Molecular Collisions, Part B, Plenum, New York, 1976.
[59] D.F. Coker, Computer simulation methods for nonadiabatic dynamics in condensed systems, in: M.P. Allen, D.J. Tildesley (Eds.), Computer Simulation in Chemical Physics, Kluwer, Dordrecht, 1993, pp. 315–377.
[60] J.C. Tully, J. Chem. Phys. 93 (1990) 1061.
[61] S. Hammes-Schiffer, J.C. Tully, J. Chem. Phys. 101 (1994) 4657.
[62] D.F. Coker, L. Xiao, J. Chem. Phys. 102 (1995) 496.
[63] V.S. Batista, D.F. Coker, J. Chem. Phys. 105 (1996) 4033.
[64] V.S. Batista, D.F. Coker, J. Chem. Phys. 106 (1997) 6923.
[65] E. Neria, A. Nitzan, R.N. Barnett, U. Landman, Phys. Rev. Lett. 67 (1991) 1011.
[66] E. Neria, A. Nitzan, J. Chem. Phys. 99 (1993) 1109.
[67] E.R. Bittner, P.J. Rossky, J. Chem. Phys. 103 (1995) 8130.
[68] B.J. Schwartz, E.R. Bittner, O.V. Prezhdo, P.J. Rossky, J. Chem. Phys. 104 (1996) 5942.
[69] E. Bittner, P. Rossky, J. Chem. Phys. 107 (1997) 8611.
[70] E.J. Heller, J. Chem. Phys. 75 (1981) 2923.
[71] U. Müller, G. Stock, J. Chem. Phys. 107 (1997) 6230.
[72] W. Pauli, General Principles of Quantum Mechanics, Springer-Verlag, New York, 1980, pages 86–87, translated by P. Achuthan, K. Venkatesan.
[73] R.K. Preston, J.C. Tully, J. Chem. Phys. 54 (1971) 4297.
[74] J.C. Tully, J. Chem. Phys. 59 (1973) 5122.
[75] L. Xiao, D. Coker, J. Chem. Phys. 100 (1994) 8646.
[76] T.J. Martinez, Chem. Phys. Lett. 272 (1997) 139.
[77] A.I. Krylov, R.B. Gerber, R.D. Coalson, J. Chem. Phys. 105 (1996) 4626.

[78] A. Krylov, R. Gerber, J. Chem. Phys. 106 (1997) 6574.
[79] D.C. Rappaport, The Art of Molecular Dynamics Simulation, Cambridge University Press, New York, 1995.
[80] P.L.A. Popelier, A.J. Stone, Mol. Phys. 82 (1994) 411.
[81] J. Faeder, R. Parson, in preparation.
[82] C.G. Gray, K.E. Gubbins, Theory of Molecular Fluids, volume 1, Clarendon, Oxford, 1984.
[83] K.P. Huber, G. Herzberg, Molecular Spectra and Molecular Structure. IV. Constants of Diatomic Molecules, Van Nostrand, New York, 1979.